RESEARCH ARTICLE | APRIL 17 2025

Schottky barrier formation and band realignment of rare-earth tritelluride charge density wave material–semiconductor interfaces

Kentaro Yumigeta ; Jan Kopaczek ; Rounak Banerjee ; Seyed Tohid Rajaei Moosavy; Anvesh Yarra; Blake Povilus ; Hayley Ruddick ; Renee Sailus ; Mukesh Kumar ; Sushant Lakhavade ; Yunbo Ou ; Zafer Mutlu ; Seth Ariel Tongay

Appl. Phys. Lett. 126, 151602 (2025)
https://doi.org/10.1063/5.0253262

Applied Physics Letters ARTICLE pubs.aip.org/aip/apl

Schottky barrier formation and band realignment of rare-earth tritelluride charge density wave material–semiconductor interfaces

Cite as: Appl. Phys. Lett. **126**, 151602 (2025); doi: 10.1063/5.0253262
Submitted: 16 December 2024 · Accepted: 5 April 2025 ·
Published Online: 17 April 2025

View Online Export Citation CrossMark

Kentaro Yumigeta,[1,2] Jan Kopaczek,[2,3] Rounak Banerjee,[2] Seyed Tohid Rajaei Moosavy,[2] Anvesh Yarra,[2] Blake Povilus,[2] Hayley Ruddick,[2] Renee Sailus,[2] Mukesh Kumar,[2] Sushant Lakhavade,[2] Yunbo Ou,[2] Zafer Mutlu,[1] and Seth Ariel Tongay[1,a)]

AFFILIATIONS

[1]Department of Materials Science & Engineering, University of Arizona, Tucson, Arizona 85721, USA
[2]Materials Science and Engineering, School for Engineering of Matter, Transport and Energy, Arizona State University, Tempe, Arizona 85287, USA
[3]Department of Semiconductor Materials Engineering, Faculty of Fundamental Problems of Technology, Wrocław University of Science and Technology, Wybrzeże Wyspiańskiego 27, 50-370 Wrocław, Poland

[a)]**Author to whom correspondence should be addressed:** stongay@asu.edu

ABSTRACT

We investigated the formation of Schottky barriers at the interface between rare-earth tritelluride (RTe$_3$) crystals and n-type silicon (n-Si) substrates. This study explores the rectifying characteristics of RTe$_3$/n-Si junctions (R = Dy, Ho, Er) and their relation to the charge density wave (CDW) transition. Using the thermionic emission model, we analyzed current–voltage (I–V) measurements to obtain the Schottky barrier height (ϕ_{SBH}) and the ideality factor (η). The temperature dependence of the extracted ϕ_{SBH} and η reveals kink features near the CDW transition temperature. The Schottky–Mott model is employed to explain these kink features in the derivatives of ϕ_{SBH} and $1/\eta$ and attributes them to changes in the work function of RTe$_3$ during the CDW transition. Our findings suggest that Schottky junctions can be utilized to probe the electronic states of RTe$_3$, enabling potential RTe$_3$ device applications in electronics and optoelectronics.

Two-dimensional (2D) materials have the potential to replace conventional materials in next-generation electronic devices due to their atomic scale thicknesses and their intriguing physical and chemical properties arising from low dimensionality. Therefore, it is essential to study the interfacial phenomena of heterojunctions when integrating 2D materials into current device fabrication processes. Schottky junctions, comprised of a metal–semiconductor junction that exhibits rectifying behavior, are critical interface structures for developing and understanding the performance of 2D material-based devices. An idealized model of the Schottky junction solely depends on the intrinsic electronic structures of the metal and semiconductor constituents. However, predicting the characteristics of Schottky barriers at metal–semiconductor interfaces is made challenging by Fermi level pinning (FLP), wherein the Fermi level is pinned at a particular energy level at the interface and cannot shift to an anticipated equilibrium position. The simple Schottky–Mott rule fails to consider more complicated effects, such as metal-induced gap states (MIGS) and bond polarizations.

Rare-earth tritellurides (RTe$_3$, R = La–Nd, Sm, Gd–Tm) comprise a class of 2D van der Waals (vdW) materials [Fig. 1(a)]. Crystalline RTe$_3$ demonstrate a wide variety of electronic and magnetic properties, with many members of this family exhibiting antiferromagnetic order (except for LaTe$_3$, which has no 4f electrons and is non-magnetic). These materials possess tunable charge density wave (CDW) states,[1–3] high carrier mobility,[4–6] superconductivity induced by intercalation and high-pressure, and magnetic properties stemming from the rare-earth elements,[5,7–11] making them candidates for next-generation electronic, optoelectronic, and spintronic devices. The CDW transition temperature of RTe$_3$ varies as a function of the rare-earth element, spanning from 245 K in TmTe$_3$ to 600 K in LaTe$_3$, demonstrating their extensive range of tunable properties.[1,12–15] RTe$_3$ materials are also among the few examples of vdW magnets with high metallicity, extending the electron regime of such magnets alongside insulating antiferromagnetic FePS$_3$,[16–18] ferromagnetic CrI$_3$,[19] Cr$_2$Ge$_2$Te$_6$,[20] and Fe$_3$GeTe$_2$,[21,22] potentially making them essential components for device applications.

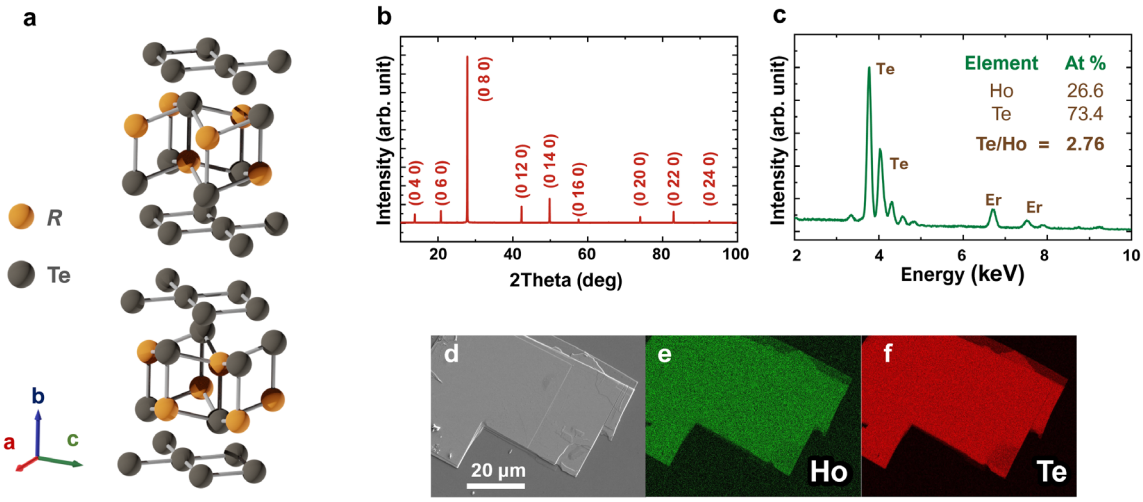

FIG. 1. (a) The crystal structure of $R\text{Te}_3$. (b) The XRD spectrum of single crystal HoTe_3. (c) The EDS spectrum, (d) SEM image, and EDS mapping of (e) Ho and (f) Te.

Although Schottky junctions of 2D vdW materials have been studied in several materials,[23–26] including some CDW materials,[27,28] no studies have yet been reported on $R\text{Te}_3$ heterojunctions. In this paper, we investigate Schottky junctions consisting of $R\text{Te}_3$ and *n*-type doped Si (*n*-Si) substrates by performing temperature-dependent current–voltage (*I*–*V*) measurements on DyTe_3, HoTe_3, and ErTe_3. Our results indicate that Schottky barriers are sensitive to the CDW formation in $R\text{Te}_3$ and can serve as interface-state probes, offering insight into the electronic properties of $R\text{Te}_3$.

The $R\text{Te}_3$ single crystals (R = Dy, Ho, Er) were synthesized using self-flux technique. Each growth contained a 5 g mixture of rare-earth metal (99.9%, Alfa Aesar) and tellurium (99.999%, Alfa Aesar) at the ratio of *R*:Te = 3:97 and was sealed in a quartz ampoule with quartz wool under 10^{-6} Torr. The ampoule was heated at a rate of 30 °C/h to 800 °C and held for 12 h. Afterward, the temperature was slowly reduced at the rate of 3 K/h to 550 °C, and the excess flux removed using a centrifuge. The ampoule was opened in a glovebox, and the ~5 mm-sized crystals were kept in an inert nitrogen environment to avoid oxidation. For energy-dispersive x-ray spectroscopy (EDS), Raman spectroscopy, and electric transport measurements, the crystals were exfoliated down to 50–100 nm thicknesses by mechanical exfoliation using the established micromechanical exfoliation. At this thickness range, the properties of the material are not significantly affected by its reduced thickness.[29]

The characterization of the synthesized crystals is shown in Figs. 1(b) and 1(f) for HoTe3 as a representative example. The crystal structure was characterized by x-ray diffraction (XRD) using a Malvern PANalytical Aeris with Cu Kα radiation ($\lambda = 1.541\,84$ Å) [Fig. 1(b)]. The XRD spectrum showed sharp (0 1 0) reflections, indicative of the out-of-plane b-axis direction. The lattice constants were consistent with reported values.[1–3] Scanning electron microscopy (SEM) and EDS were performed with an accelerating voltage of 20 kV. The EDS spectrum [Fig. 1(c)] showed an R to Te ratio close to the ideal 1:3 stoichiometry, with a measured value of 2.76. This slight deviation suggests the possible presence of a small number of Te vacancies. Figure 1(d) shows SEM imaging of exfoliated samples, and the EDS mapping images shown in Figs. 1(e) and 1(f) reveal uniform distribution of rare-earth and tellurium atoms across the entire crystal.

The samples used for *I*–*V* measurements were prepared by deterministic transfer of mechanically exfoliated crystals [Figs. 2(a) and 2(b)]. The transfer procedure is illustrated in the supplementary material (Fig. S1). The polycarbonate (PC) solution was prepared by mixing 5% PC in chloroform to produce a homogeneous solution. The $R\text{Te}_3$ crystals were mechanically exfoliated onto PC-coated glass sides. Prior to transferring the exfoliated crystal, the Au/Cr electrode (100 nm of Au and 20 nm of Cr as a wetting layer) was deposited onto as-received Si (001) (*n*-type 8×10^{14} to 1×10^{15} cm^{-3}) wafers with a 300 nm thick oxide layer (SiO_2). The exposed SiO_2 was etched with a buffered oxide etchant (BOE) consisting of 6 NH_4F:1 HF.

Prior to the $R\text{Te}_3$ flake transfer, the current between the top electrode and the Si substrate was measured. The leakage current was confirmed to be below the detection limit of our measurement system (10 pA), indicating that leakage current is not a significant factor in our measurement.

The exfoliated $R\text{Te}_3$ crystal and PC film were transferred onto the exposed Si surface and the deposited Au/Cr electrode. The PC film was left on top of the device to impede oxidation of the $R\text{Te}_3$ crystal. The transfer procedure was completed in less than 30 min to minimize air exposure. Ohmic contact to the Si substrate was achieved by Cr deposition onto the backside of the Si substrate followed by annealing at 500 °C for 10 min to form Cr silicide at the interface. The *I*–*V* characteristic of this Ohmic contact used in this study is shown in the supplementary material (Fig. S2).

The temperature-dependent *I*–*V* measurements were performed using a Janis cryostat over a temperature range of 30–320 K, with measurements taken at 1 K intervals. The voltage control and current readings were obtained using a Keithley 2400 SourceMeter.

The Schottky–Mott model represents the bands diagram of a metal–semiconductor junction [Fig. 2(c)] when the FLP can be ignored. According to this model, the Schottky barrier height ϕ_{SBH} can be determined via the work function of the metal and the electron affinity of the semiconductor as described by $\phi_{SBH} = \phi_M - \chi$. Below

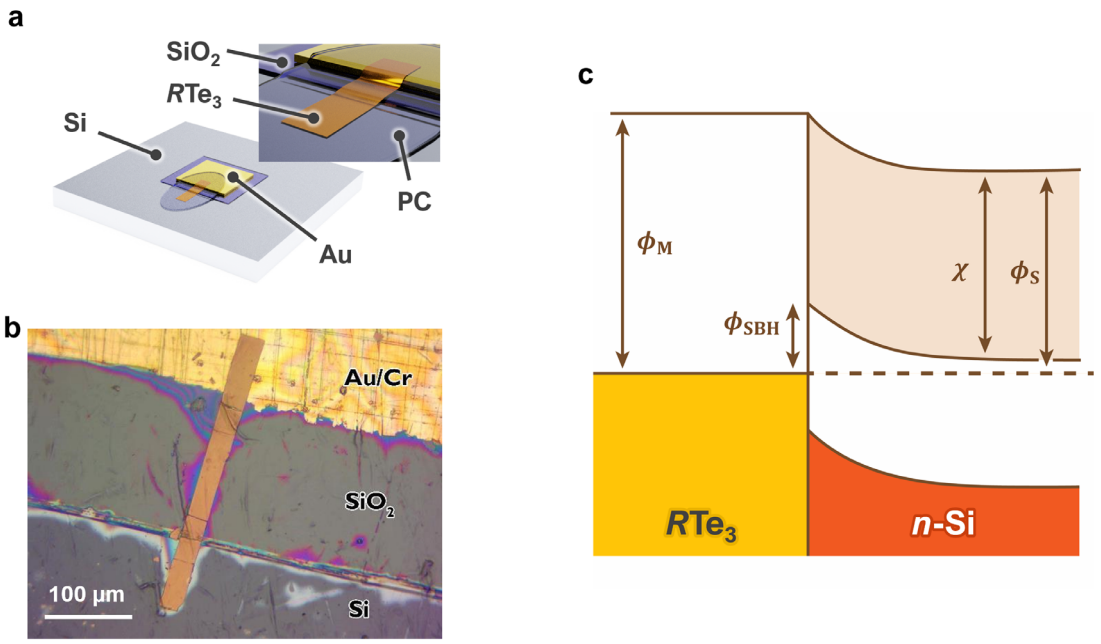

FIG. 2. (a) Geometry of the $R\mathrm{Te_3}$/*n*-Si Schottky junction device. (b) Optical image of the $\mathrm{ErTe_3}$/*n*-Si Schottky junction device. (c) Band diagram of a Schottky junction formed by metallic $R\mathrm{Te_3}$ and *n*-Si substrate. ϕ_{SBH} is the Schottky barrier height, ϕ_M is the work function of $R\mathrm{Te_3}$, ϕ_s is the work function of *n*-Si, χ is the electron affinity of *n*-Si. The dashed line represents the Fermi level. In the Schottky–Mott model, below the CDW transition temperature of $R\mathrm{Te_3}$, the work function increases due to the CDW gap opening at the Fermi level of $R\mathrm{Te_3}$, and the Schottky barrier height increases.

the CDW transition temperature of $R\mathrm{Te_3}$, the work function of $R\mathrm{Te_3}$ increases due to the CDW gap opening at the Fermi level; therefore, the Schottky barrier height is expected to increase.

The temperature dependence of the out-of-plane resistivity measured using a four-probe configuration is shown in Fig. 3. The transition temperatures determined from the derivatives of the resistivity vs temperature graph were $T_{CDW1} = 263$ K, $T_{CDW2} = 157$ K for $\mathrm{ErTe_3}$, $T_{CDW1} = 285$ K, $T_{CDW2} = 110$ K for $\mathrm{HoTe_3}$, and $T_{CDW1} = 307$ K, $T_{CDW2} = 51$ K for $\mathrm{DyTe_3}$, respectively. The derivatives used to determine the transition temperatures are shown in the supplementary material (Figs. S3–S6). The transition temperatures are consistent with our Raman spectroscopy study (Fig. 4) and reported results.[30–32]

$R\mathrm{Te_3}$ crystals exhibit two CDW transitions characterized by distinct wavevectors along the *c*-axis (T_{CDW1}) and *a*-axis (T_{CDW2}). The CDW transition temperatures of these $R\mathrm{Te_3}$ crystals have been verified by examining the temperature dependence of Raman spectra for T_{CDW1}, as well as resistivity measurements for both T_{CDW1} and T_{CDW2}.

Taking $\mathrm{HoTe_3}$ as an example, its temperature-dependent Raman spectra are shown in Fig. 4(a). A peak around 52 $\mathrm{cm^{-1}}$ at 88 K corresponds to the CDW amplitude mode and shifts toward lower energies (softens) as the temperature rises. This peak moves to zero frequency and disappears above the CDW transition temperature. At lower temperatures, as the intensity of the CDW amplitude mode diminishes, the Raman shift becomes temperature-independent, and the intensity of the peak near 60 $\mathrm{cm^{-1}}$ strengthens and blueshifts. This observed anti-crossing behavior arises from the interaction between the CDW amplitude mode and the phonon mode, aligning with previous studies[30,31,33]

The Ginzburg–Landau model can describe the temperature dependence of the CDW mode as $\omega_{CDW} = \omega_0 \times (1 - \frac{T}{T_{CDW}})^{\beta}$,[30,31,34] where ω_{CDW} denotes the frequency of the CDW mode, ω_0 represents the CDW amplitude mode's frequency at low temperature,

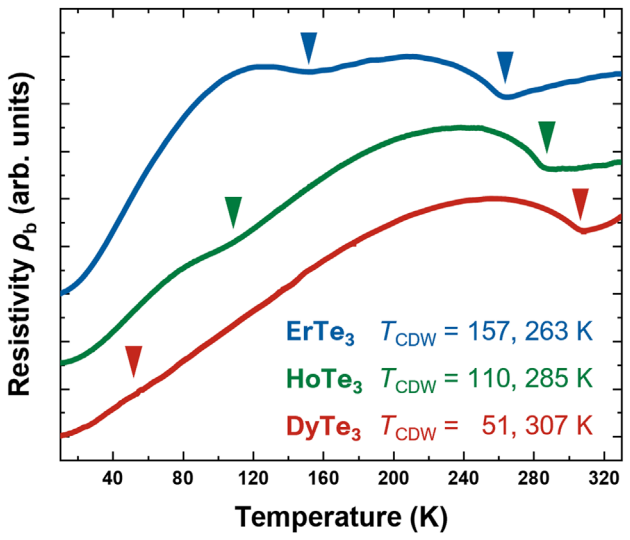

FIG. 3. Out-of-plane resistivity vs temperature of $\mathrm{DyTe_3}$, $\mathrm{HoTe_3}$, and $\mathrm{ErTe_3}$. The current is oriented along the *b*-axis direction (out-of-plane). The CDW transition temperatures are marked by triangles for each compound. The data are offset for clarity.

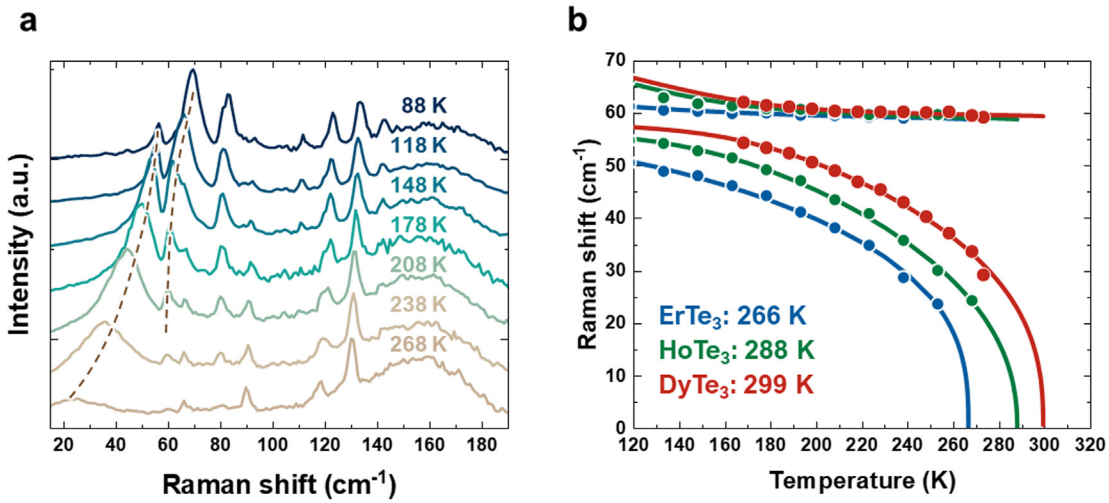

FIG. 4. (a) Raman spectra of $HoTe_3$ as a function of temperature, measured from 88 to 268 K in 30 K intervals. Dotted lines indicate the CDW amplitude mode and an associated phonon mode used for fitting. (b) The variation in temperature for both the CDW amplitude mode and the coupled phonon mode of $DyTe_3$, $HoTe_3$, and $ErTe_3$. Solid lines demonstrate the fits based on the interaction between the phonon mode and the amplitude mode, following the Ginzburg–Landau temperature dependence coupled with a phonon mode.

and β is a critical exponent. The CDW amplitude mode and phonon mode (ω_{ph}) interact through a coupling constant (δ), which can be expressed as a matrix $\begin{pmatrix} \omega_{CDW} & \delta \\ \delta & \omega_{ph} \end{pmatrix}$. The eigenvalues of this matrix correspond to the vibrational frequencies observed in Raman spectroscopy. The data points presented in Fig. 4(b) were used for fitting purposes, while those at lower temperatures were excluded due to the observed coupling with another peak around 80 cm^{-1}, resulting in a deviation from the two-mode coupling model. The CDW transition temperatures of $ErTe_3$, $HoTe_3$, and $DyTe_3$ were determined by fitting the Ginzburg–Landau model coupled with the phonon mode shown in Fig. 4(b). The fittings yield T_{CDW1} values of 266 K for $ErTe_3$, 288 K for $HoTe_3$, and 299 K for $DyTe_3$.

The *I*–*V* curves for RTe_3/*n*-Si junctions were measured by applying the voltage between the Au electrode and the n-Si substrate. Figure 5 shows the measured *I*–*V* curves for $ErTe_3$ as an example of the studied RTe_3 materials. These curves demonstrate rectifying characteristics, indicative of Schottky barrier formation at the interface between RTe_3 crystals and the *n*-Si substrate. The *I*–*V* characteristics of the other RTe_3/Si and Au/Si junctions, along with that of a reference Au/Si Schottky junction fabricated by direct deposition of Au onto Si, are shown in the supplementary material (Figs. S8–S10). To evaluate the Schottky barrier height ϕ_{SBH} and the ideality factor η, the *I*–*V*

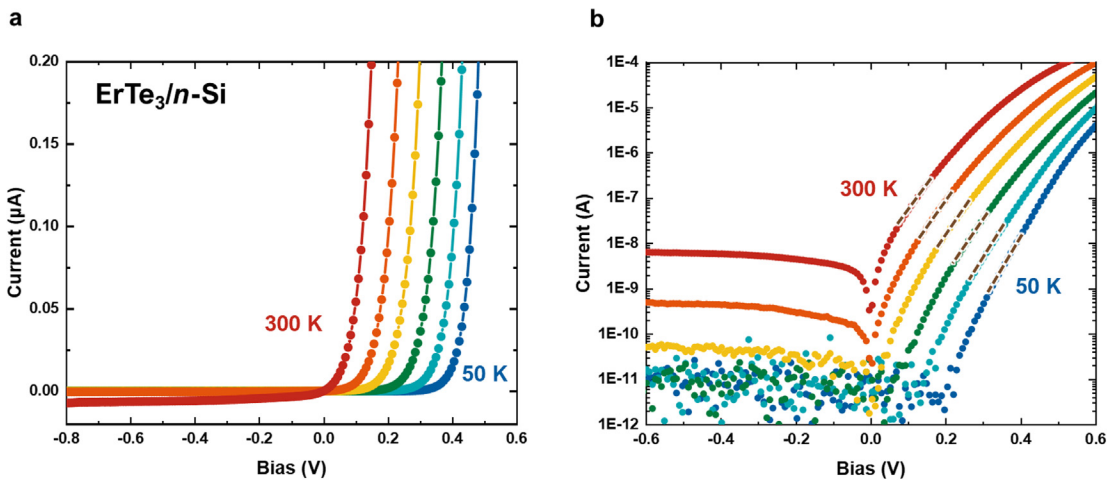

FIG. 5. *I*–*V* characteristics of $ErTe_3$/*n*-Si Schottky junction at different temperatures (a) in the linear scale and (b) in the semilogarithmic scale. The data shown are selected as examples at 50 K intervals between 50 and 300 K. The dotted lines in the semilogarithmic plot represent the linear parts used for the calculation of the Schottky barrier height ϕ_{SBH} and the ideality factor η.

measurements were fitted to the thermionic emission model, providing insights into current transport across the Schottky junction. The model is represented by the equation

$$I(T,V) = I_0(T)\left[\exp\left(\frac{eV}{\eta k_B T}\right) - 1\right]. \quad (1)$$

Here, $I(T, V)$ is the current as a function of temperature T and applied voltage V, e is the elementary charge, η is the ideality factor, and k_B is the Boltzmann constant. The saturation current $I_0(T)$ is defined as

$$I_0(T) = SA^*T^2\exp\left(-\frac{e\phi_{SBH}}{k_B T}\right). \quad (2)$$

In this equation, S is the diode area, ϕ_{SBH} is the Schottky barrier height, and $A^* = \frac{4\pi q m^* k^2}{h^3}$ is the Richardson constant, which equals 112 A/cm^{2}K^2 for n-type Si. The ideality factor, η, offers insight into the primary current transport mechanism within the Schottky junction. An ideality factor close to 1 indicates that thermionic emission mainly governs current transport, whereas values significantly greater than 1 suggest additional current transport mechanisms, such as tunneling or recombination.[35]

A linear fit was achieved by plotting $\ln(I)$ against V. The slope of this linear fit was used to determine the ideality factor η, and the y-intercept was used to calculate the Schottky barrier height ϕ_{SBH}. The temperature dependences of η and ϕ_{SBH} were determined through multiple temperature scans and averaged to reduce noise. The standard errors of the determined η and ϕ_{SBH} are shown in the supplementary material (Figs. S11–S14). The derivatives of η and ϕ_{SBH} were smoothed via the Savitzky–Golay method using a 51-point window (corresponding to a 51 K temperature range) and a polynomial order of 2. To mitigate device-to-device variations and the impact of slow RTe_3 degradation caused by trace amounts of residual air in the vacuum system, data were acquired from multiple devices. The extracted ϕ_{SBH} and η exhibit temperature dependency as shown in Fig. 6. Additionally, the values of ϕ_{SBH} and η for Au, a material

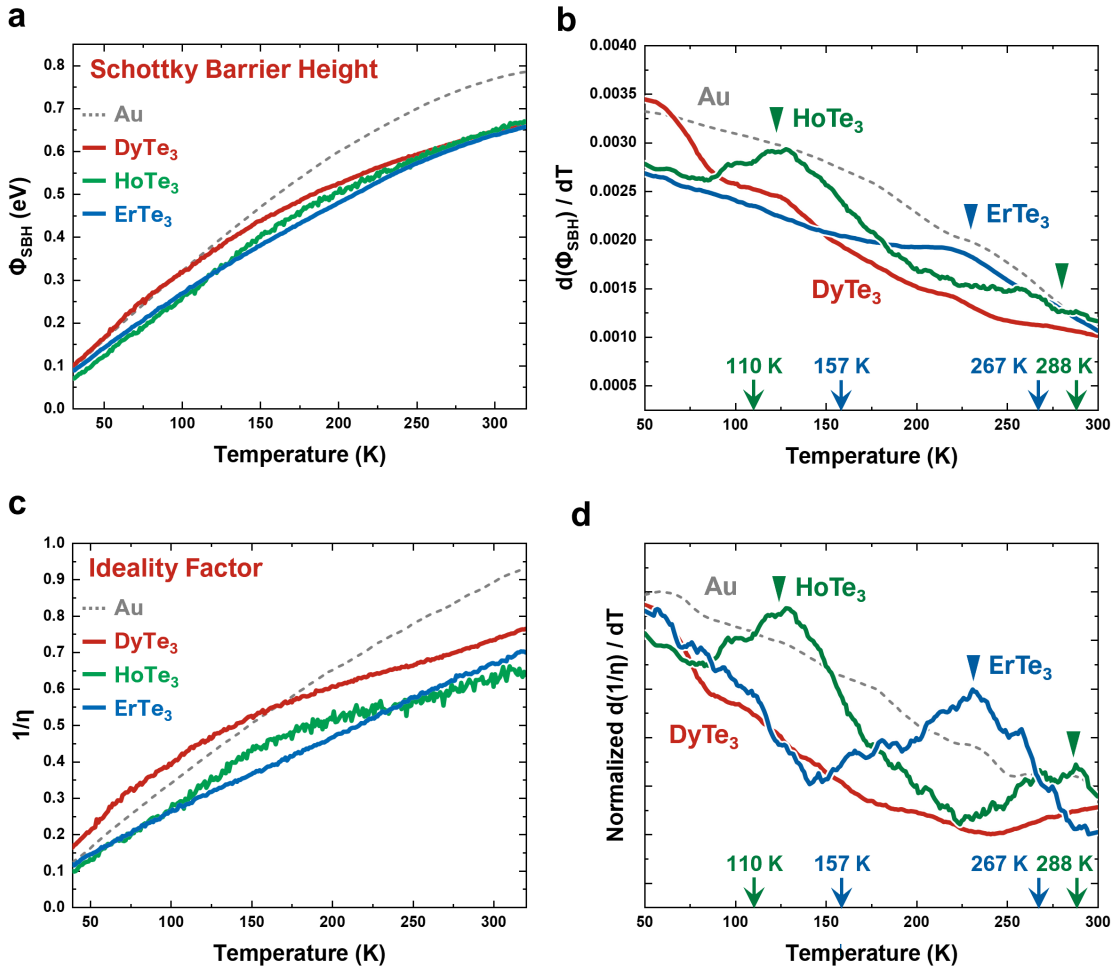

FIG. 6. (a) and (b) Schottky barrier height ϕ_{SBH} and the derivative of ϕ_{SBH} as a function of temperature. (c) and (d) Ideality factor η and the derivative of η as a function of temperature. The y-axis scale of d η/dT was individually optimized for $DyTe_3$, $HoTe_3$, and $ErTe_3$ to highlight the kink associated with the CDW transition. Triangles represent the CDW transition for each RTe_3 compound.

without a CDW transition, are shown by yellow dashed lines for comparison. Figure 6(a), the Schottky barrier height ϕ_{SBH}, does not display evident kinks as observed in other CDW/3D material Schottky junctions reported by other groups.[27,28] Nonetheless, kinks are clearly visible in the derivative of ϕ_{SBH}, shown in Fig. 6(b). These kinks are marked by a colored triangle for each RTe$_3$. For ErTe$_3$, a kink occurs around 228 K, while for HoTe$_3$, two kinks appear around 129 and 254 K. These temperatures are adjacent to the CDW transition temperatures measured by electric transport measurements and temperature-dependent Raman spectroscopy, implying that these kinks originate from the CDW transition. ErTe$_3$ displays a sole kink in the derivate of ϕ_{SBH}, while the out-of-plane resistivity indicates two CDW transition temperatures. This discrepancy might arise because the two transition temperatures of ErTe$_3$ are close, making it difficult to distinguish the two kinks in the derivative of ϕ_{SBH} of ErTe$_3$. The CDW transition temperature of DyTe$_3$ was not within the investigated range, and therefore a distinct kink was not observed.

The kinks are more pronounced in the derivative of $1/\eta$. Figures 6(c) and 6(d) depict the temperature dependence of $1/\eta$ and the derivative of $1/\eta$, respectively. For ErTe$_3$, a kink appears at 233 K, while for HoTe$_3$, two kinks emerge around 130 and 283 K. Similar to the behavior of ϕ_{SBH}, ErTe$_3$ only exhibits a single kink, possibly because its two transition temperatures are close and thus difficult to differentiate. The temperatures of the kinks in the derivative of $1/\eta$ are similar to the temperatures obtained from the derivative of ϕ_{SBH}. It is worth noting that DyTe$_3$ shows a dip in the derivative of $1/\eta$, which is not observed in the derivative of ϕ_{SBH}. This possibly implies the kink exists near 300 K, matching the CDW transition temperature determined by electric transport measurement and the reported values in the literature.[30–32]

The kink features observed exclusively in RTe$_3$/n-Si and not in Au/n-Si junctions initially suggest that the work function shift of RTe$_3$ influences both the Schottky barrier height and the ideality factor. However, a more careful interpretation reveals other potential influences. If the CDW transition alters the density of interfacial states and the strength of FLP, the kinks in the Schottky junction properties may arise by the change of FLP rather than the change in the RTe$_3$ work function. The models of FLP can be classified by its origin being extrinsic or intrinsic.

The extrinsic origins result from imperfections such as vacancies, impurities, and residues at the interface, and the models describing the extrinsic origins include the disorder-induced gap state (DIGS)[36] and the unified defect model (UDM).[37] DIGS is described by weakened energy splitting between bonding and antibonding states resulting from disrupted crystal lattice periodicity, whereas UDM originates from the formation of defects and antistites, which create discrete defect states. As both models originate from the semiconductor component and not the metal, these effects are negligible in our samples.

A small degree of surface oxidation during sample preparation is inevitable. The oxide layer forms a disordered structure rather than a crystalline oxide at the interface,[38] which might promote FLP through mechanisms such as DIGS and UDM. ErTe$_3$ exhibits a higher oxidation rate compared to DyTe$_3$ and HoTe$_3$, which may explain the less pronounced features observed in ErTe$_3$ at the transition temperature compared to DyTe$_3$ and HoTe$_3$. However, since this is also an extrinsic origin of FLP, it similarly cannot account for the kinks observed at the CDW transition temperature.

The intrinsic origins include Metal-induced gap state (MIGS)[39] and the bond polarization model.[40] MIGS is formed in the Si bandgap by the penetration of the electron wave function of RTe$_3$. While MIGS at 2D metal/2D semiconductor junctions are suppressed, strong FLP has been observed in many 2D/3D material junctions.[26,41–44] It is possible that MIGS are formed at the RTe$_3$/n-Si interface. However, MIGS has a dependence on the semiconductor used, and the effect of the metal is minimal. Therefore, the FLP contribution to the change in the work function of RTe$_3$ arising from MIGS is negligible.

The band polarization model can be described by $\phi_{SBH} = \phi_M - \chi_S + \frac{-q^2 N_B d_{MS}}{\epsilon} Q_S$, where N_B is the density of bonds at the metal/semiconductor interface, d_{MS} is the distance between metal and semiconductor atoms, Q_S is the change in charge of semiconductor atoms at the interface.[40] Therefore, this model depends on the metal used through the density of bonds at the metal/semiconductor interface, the distance between the metal and semiconductor atoms, and the metal work function. Since lattice distortion in the CDW state is minimal, the changes in chemical bonding and the distance between the metal/semiconductor atoms at the interface on the FLP during CDW formation are also minimal. Another possible explanation for the observed changes stems from the modulation of interfacial dielectric properties during the CDW transition, as reported in 1 T-TaS$_2$.[28] However, this possibility can be ruled out because the carrier density of RTe$_3$ stays significantly higher than that of n-Si. Based on this analysis, the kinks can be attributed to the change in the work function of RTe$_3$ originating from the CDW transition.

The kink features observed in the derivates of both the Schottky barrier height ϕ_{SBH} and ideality factor η can be qualitatively justified using the Schottky–Mott mode. The Schottky barrier height is determined by the equation $\phi_{SBH} = \phi_m - \chi$. As the temperature decreases and the material enters the CDW state, ϕ_m increases, resulting in a larger ϕ_{SBH}. This increase causes a downward deflection in the derivative of ϕ_{SBH}, observed on the lower temperature side of the CDW transition temperature, as illustrated in Figs. 6(a) and 6(b).

The ideality factor η decreases (corresponding to an increase in $1/\eta$) below the CDW transition temperature, as displayed in Figs. 6(c) and 6(d). This observation suggests an increased contribution from thermionic transport. A possible explanation for this behavior is that the Schottky barrier height increases below the CDW transition temperature, thereby reducing the tunneling probability.

In conclusion, our study has shown demonstrated heterojunctions with RTe$_3$ and the formation of Schottky junctions for RTe$_3$/n-Si (R = Dy, Ho, Er). The temperature dependence of Schottky barrier height and ideality factor in RTe$_3$/n-Si heterostructures has yielded insights into the effects of the CDW transition on Schottky junction properties. The kink features observed in the derivatives of both Schottky barrier height and ideality factor can be attributed to changes in the work function of RTe$_3$ during the CDW transition. These kink temperatures were found to be close to the bulk CDW transition temperatures. Our analysis has ruled out the impact of MIGS, band polarization, and modulation of interfacial dielectric properties as the primary sources for the observed kinks.

Our findings highlight the significance of CDW transitions on the Schottky barrier height and ideality factor, which has important implications for developing devices based on these heterostructures. Furthermore, this work demonstrates the potential of Schottky junctions as a tool for probing electronic states in RTe$_3$ materials and broadens the scope of their application in electronic devices.

See the supplementary material for sample preparation, measurements, methodology, and error analysis.

This study was primarily conducted during the author's Ph.D. research at the Department of Materials Science and Engineering, Arizona State University. The final analysis and manuscript preparation were completed while the author was affiliated with the Department of Materials Science and Engineering, University of Arizona. S.T. acknowledges primary support from NSF CBET 23301109 (environmental studies of tritellurides and development of the crystals). S.T. acknowledges partial support from NSF DMR 2206987 (magnetic tests) and Applied Materials Inc. Z.M. acknowledges support from NSF No. CHE-2235143. J.K. acknowledges support within the Bekker program from the Polish National Agency for Academic Exchange.

AUTHOR DECLARATIONS

Conflict of Interest

The authors have no conflicts to disclose.

Author Contributions

Kentaro Yumigeta: Formal analysis (lead); Investigation (lead); Methodology (lead); Resources (equal); Visualization (lead); Writing – original draft (lead). **Jan Kopaczek:** Funding acquisition (supporting); Investigation (equal); Writing – review & editing (equal). **Rounak Banerjee:** Formal analysis (supporting); Investigation (equal); Visualization (supporting). **Seyed Tohid Rajaei Moosavy:** Resources (equal). **Anvesh Yarra:** Resources (equal). **Blake Povilus:** Resources (equal). **Hayley Ruddick:** Resources (equal). **Renee Sailus:** Investigation (supporting). **Mukesh Kumar:** Investigation (supporting). **Sushant Lakhavade:** Investigation (supporting). **Yunbo Ou:** Investigation (supporting); Writing – review & editing (equal). **Zafer Mutlu:** Funding acquisition (supporting); Supervision (equal); Writing – review & editing (equal). **Seth Ariel Tongay:** Conceptualization (equal); Funding acquisition (equal); Supervision (equal); Writing – review & editing (equal).

DATA AVAILABILITY

The data that support the findings of this study are available within the article and its supplementary material.

REFERENCES

[1]N. Ru, C. L. Condron, G. Y. Margulis, K. Y. Shin, J. Laverock, S. B. Dugdale, M. F. Toney, and I. R. Fisher, "Effect of chemical pressure on the charge density wave transition in rare-earth tritellurides RTe_3," Phys. Rev. B **77**(3), 035114 (2008).

[2]J. F. Cannon and H. T. Hall, "High-pressure, high-temperature syntheses of selected lanthanide-tellurium compounds," Inorg. Chem. **9**(7), 1639–1643 (1970).

[3]C. D. Malliakas and M. G. Kanatzidis, "Divergence in the behavior of the charge density wave in $RETe_3$ (RE = rare-earth element) with temperature and RE element," J. Am. Chem. Soc. **128**(39), 12612–12613 (2006).

[4]S. Lei, J. Lin, Y. Jia, M. Gray, A. Topp, G. Farahi, S. Klemenz, T. Gao, F. Rodolakis, J. L. McChesney, C. R. Ast, A. Yazdani, K. S. Burch, S. Wu, N. P. Ong, and L. M. Schoop, "High mobility in a van der Waals layered antiferromagnetic metal," Sci. Adv. **6**(6), eaay6407 (2020).

[5]J. S. Liu, S. C. Huan, Z. H. Liu, W. L. Liu, Z. T. Liu, X. L. Lu, Z. Huang, Z. C. Jiang, X. Wang, N. Yu, Z. Q. Zou, Y. F. Guo, and D. W. Shen, "Electronic structure of the high-mobility two-dimensional antiferromagnetic metal $GdTe_3$," Phys. Rev. Mater. **4**(11), 114005 (2020).

[6]M. Watanabe, R. Nakamura, S. Lee, T. Asano, T. Ibe, M. Tokuda, H. Taniguchi, D. Ueta, Y. Okada, K. Kobayashi, and Y. Niimi, "Shubnikov-de-Haas oscillation and possible modification of effective mass in $CeTe_3$ thin films," AIP Adv. **11**(1), 015005 (2021).

[7]Y. Iyeiri, T. Okumura, C. Michioka, and K. Suzuki, "Magnetic properties of rare-earth metal tritellurides RTe_3 (R=Ce,Pr,Nd,Gd,Dy)," Phys. Rev. B **67**(14), 144417 (2003).

[8]N. Ru, J. H. Chu, and I. R. Fisher, "Magnetic properties of the charge density wave compounds RTe_3 (R=Y, La, Ce, Pr, Nd, Sm, Gd, Tb, Dy, Ho, Er, and Tm)," Phys. Rev. B **78**(1), 012410 (2008).

[9]Q. Guo, D. Bao, L. J. Zhao, and S. Ebisu, "Novel magnetic behavior of antiferromagnetic $GdTe_3$ induced by magnetic field," Physica B **617**, 413153 (2021).

[10]K. Deguchi, T. Okada, G. F. Chen, S. Ban, N. Aso, and N. K. Sato, "Magnetic order of rare-earth tritelluride $CeTe_3$ at low temperature," J. Phys.: Conf. Ser. **150**(4), 042023 (2009).

[11]Z. Yang, A. J. Drew, S. van Smaalen, N. van Well, F. L. Pratt, G. B. G. Stenning, A. Karim, and K. Rabia, "Multiple magnetic-phase transitions and critical behavior of charge-density wave compound $TbTe_3$," J. Phys.: Condens. Matter **32**(30), 305801 (2020).

[12]A. Kogar, A. Zong, P. E. Dolgirev, X. Shen, J. Straquadine, Y.-Q. Bie, X. Wang, T. Rohwer, I. C. Tung, Y. Yang, R. Li, J. Yang, S. Weathersby, S. Park, M. E. Kozina, E. J. Sie, H. Wen, P. Jarillo-Herrero, I. R. Fisher, X. Wang, and N. Gedik, "Light-induced charge density wave in $LaTe_3$," Nat. Phys. **16**(2), 159–163 (2020).

[13]K. Yumigeta, Y. Qin, H. Li, M. Blei, Y. Attarde, C. Kopas, and S. Tongay, "Advances in rare-earth tritelluride quantum materials: Structure, properties, and synthesis," Adv. Sci. **8**, 2004762 (2021).

[14]E. DiMasi, M. C. Aronson, J. F. Mansfield, B. Foran, and S. Lee, "Chemical pressure and charge-density waves in rare-earth tritellurides," Phys. Rev. B **52**(20), 14516–14525 (1995).

[15]A. Sacchetti, L. Degiorgi, T. Giamarchi, N. Ru, and I. R. Fisher, "Chemical pressure and hidden one-dimensional behavior in rare-earth tri-telluride charge-density wave compounds," Phys. Rev. B **74**(12), 125115 (2006).

[16]B. F. Hu, B. Cheng, R. H. Yuan, T. Dong, and N. L. Wang, "Coexistence and competition of multiple charge-density-wave orders in rare-earth tritellurides," Phys. Rev. B **90**(8), 085105 (2014).

[17]X. Wang, K. Du, Y. Y. Fredrik Liu, P. Hu, J. Zhang, Q. Zhang, M. H. S. Owen, X. Lu, C. K. Gan, P. Sengupta, C. Kloc, and Q. Xiong, "Raman spectroscopy of atomically thin two-dimensional magnetic iron phosphorus trisulfide ($FePS_3$) crystals," 2D Mater. **3**(3), 031009 (2016).

[18]J. U. Lee, S. Lee, J. H. Ryoo, S. Kang, T. Y. Kim, P. Kim, C. H. Park, J. G. Park, and H. Cheong, "Ising-type magnetic ordering in atomically thin $FePS_3$," Nano Lett. **16**(12), 7433–7438 (2016).

[19]B. Huang, G. Clark, E. Navarro-Moratalla, D. R. Klein, R. Cheng, K. L. Seyler, D. Zhong, E. Schmidgall, M. A. McGuire, D. H. Cobden, W. Yao, D. Xiao, P. Jarillo-Herrero, and X. Xu, "Layer-dependent ferromagnetism in a van der Waals crystal down to the monolayer limit," Nature **546**(7657), 270–273 (2017).

[20]C. Gong, L. Li, Z. Li, H. Ji, A. Stern, Y. Xia, T. Cao, W. Bao, C. Wang, Y. Wang, Z. Q. Qiu, R. J. Cava, S. G. Louie, J. Xia, and X. Zhang, "Discovery of intrinsic ferromagnetism in two-dimensional van der Waals crystals," Nature **546**(7657), 265–269 (2017).

[21]Y. Deng, Y. Yu, Y. Song, J. Zhang, N. Z. Wang, Z. Sun, Y. Yi, Y. Z. Wu, S. Wu, J. Zhu, J. Wang, X. H. Chen, and Y. Zhang, "Gate-tunable room-temperature ferromagnetism in two-dimensional Fe_3GeTe_2," Nature **563**(7729), 94–99 (2018).

[22]Z. Fei, B. Huang, P. Malinowski, W. Wang, T. Song, J. Sanchez, W. Yao, D. Xiao, X. Zhu, A. F. May, W. Wu, D. H. Cobden, J. H. Chu, and X. Xu, "Two-dimensional itinerant ferromagnetism in atomically thin Fe_3GeTe_2," Nat. Mater. **17**(9), 778–782 (2018).

[23]A. Di Bartolomeo, "Graphene Schottky diodes: An experimental review of the rectifying graphene/semiconductor heterojunction," Phys. Rep. **606**, 1–58 (2016).

[24]A. Di Bartolomeo, G. Luongo, F. Giubileo, N. Funicello, G. Niu, T. Schroeder, M. Lisker, and G. Lupina, "Hybrid graphene/silicon Schottky photodiode with intrinsic gating effect," 2D Mater. **4**(2), 025075 (2017).
[25]X. Miao, S. Tongay, M. K. Petterson, K. Berke, A. G. Rinzler, B. R. Appleton, and A. F. Hebard, "High efficiency graphene solar cells by chemical doping," Nano Lett. **12**(6), 2745–2750 (2012).
[26]C. Kim, I. Moon, D. Lee, M. S. Choi, F. Ahmed, S. Nam, Y. Cho, H. J. Shin, S. Park, and W. J. Yoo, "Fermi level pinning at electrical metal contacts of monolayer molybdenum dichalcogenides," ACS Nano **11**(2), 1588–1596 (2017).
[27]A. J. Li, X. Zhu, D. Rhodes, C. C. Samouce, L. Balicas, and A. F. Hebard, "van der Waals Schottky barriers as interface probes of the correlation between chemical potential shifts and charge density wave formation in 1T−$TiSe_2$ and 2H−$NbSe_2$," Phys. Rev. B **96**(12), 125301 (2017).
[28]X. Zhu, A. J. Li, G. R. Stewart, and A. F. Hebard, "Detection of charge density wave phase transitions at 1T-TaS_2/GaAs interfaces," Appl. Phys. Lett. **110**(18), 181603 (2017).
[29]S. Yang, H. Cai, B. Chen, C. Ko, V. O. Ozcelik, D. F. Ogletree, C. E. White, Y. Shen, and S. Tongay, "Environmental stability of 2D anisotropic tellurium containing nanomaterials: Anisotropic to isotropic transition," Nanoscale **9**(34), 12288–12294 (2017).
[30]M. Lavagnini, H. M. Eiter, L. Tassini, B. Muschler, R. Hackl, R. Monnier, J. H. Chu, I. R. Fisher, and L. Degiorgi, "Raman scattering evidence for a cascade evolution of the charge-density-wave collective amplitude mode," Phys. Rev. B **81**(8), 081101 (2010).
[31]Y. Chen, P. Wang, M. Wu, J. Ma, S. Wen, X. Wu, G. Li, Y. Zhao, K. Wang, L. Zhang, L. Huang, W. Li, and M. Huang, "Raman spectra and dimensional effect on the charge density wave transition in $GdTe_3$," Appl. Phys. Lett. **115**(15), 151905 (2019).
[32]H. M. Eiter, M. Lavagnini, R. Hackl, E. A. Nowadnick, A. F. Kemper, T. P. Devereaux, J. H. Chu, J. G. Analytis, I. R. Fisher, and L. Degiorgi, "Alternative route to charge density wave formation in multiband systems," Proc. Natl. Acad. Sci. U. S. A. **110**(1), 64–69 (2013).
[33]R. V. Yusupov, T. Mertelj, J. H. Chu, I. R. Fisher, and D. Mihailovic, "Single-particle and collective mode couplings associated with 1- and 2-directional electronic ordering in metallic RTe_3 (R=Ho,Dy,Tb)," Phys. Rev. Lett. **101**(24), 246402 (2008).
[34]G. Grüner, *Density Waves in Solids* (CRC Press, 2018).
[35]R. T. Tung, "Recent advances in Schottky barrier concepts," Mater. Sci. Eng., R **35**(1–3), 1–138 (2001).
[36]H. Hasegawa, "Unified disorder induced gap state model for insulator–semiconductor and metal–semiconductor interfaces," J. Vac. Sci. Technol., B: Microelectron. Nanometer Struct. **4**(4), 1130 (1986).
[37]W. E. Spicer, P. W. Chye, P. R. Skeath, C. Y. Su, and I. Lindau, "New and unified model for Schottky barrier and III–V insulator interface states formation," J. Vac. Sci. Technol. **16**(5), 1422–1433 (1979).
[38]J. Kopaczek, K. Yumigeta, A. Ibrahim, M. Y. Sayyad, S. Sinha, R. Sailus, P. Hays, S. T. R. Moosavy, S. Susarla, C. Ataca, R. Kudrawiec, and S. Tongay, "Experimental and theoretical studies of the surface oxidation process of rare-earth tritellurides," Adv. Electron. Mater. **9**, 2201129 (2023).
[39]W. Mönch, "Chemical trends of barrier heights in metal-semiconductor contacts: On the theory of the slope parameter," Appl. Surf. Sci. **92**, 367–371 (1996).
[40]R. T. Tung, "Chemical bonding and fermi level pinning at metal-semiconductor interfaces," Phys. Rev. Lett. **84**(26), 6078–6081 (2000).
[41]Y. Liu, P. Stradins, and S. H. Wei, "Van der Waals metal-semiconductor junction: Weak Fermi level pinning enables effective tuning of Schottky barrier," Sci. Adv. **2**(4), e1600069 (2016).
[42]X. Liu, M. S. Choi, E. Hwang, W. J. Yoo, and J. Sun, "Fermi level pinning dependent 2D semiconductor devices: Challenges and prospects," Adv. Mater. **34**(15), e2108425 (2022).
[43]Y. Liu, N. O. Weiss, X. Duan, H.-C. Cheng, Y. Huang, and X. Duan, "Van der Waals heterostructures and devices," Nat. Rev. Mater. **1**(9), 1 (2016).
[44]C. Gong, L. Colombo, R. M. Wallace, and K. Cho, "The unusual mechanism of partial Fermi level pinning at metal–MoS_2 interfaces," Nano Lett. **14**(4), 1714–1720 (2014).